Modelling of Hydrodynamic Cavitation with Orifice: Influence of different orifice designs

Simpson, A., & Ranade, V. V. (2018). Modelling of Hydrodynamic Cavitation with Orifice: Influence of different orifice designs. *Chemical Engineering Research and Design*, *136*, 698-711. https://doi.org/10.1016/j.cherd.2018.06.014

Published in:
Chemical Engineering Research and Design

Document Version:
Peer reviewed version

Queen's University Belfast - Research Portal:
Link to publication record in Queen's University Belfast Research Portal

Modelling of Hydrodynamic Cavitation with Orifice: Influence of different orifice designs

Alister Simpson and Vivek V. Ranade*
School of Chemistry and Chemical Engineering
Queen's University Belfast, Belfast BT9 5AG, UK
*Email: V.Ranade@qub.ac.uk

Abstract

Hydrodynamic cavitation (HC) may be harnessed to intensify a range of industrial processes, and orifice devices are one of the most widely used for HC. Despite the wide spread use, the influence of various design and operating parameters on generated cavitation is not yet adequately understood. This paper presents results of computational investigation into cavitation in different orifice designs over a range of operating conditions. Key geometric parameters like orifice thickness, hole inlet sharpness and wall angle on the cavitation behaviour is discussed quantitatively. Formulation and numerical solution of multiphase computational fluid dynamics (CFD) models are presented. The simulated results in terms of velocity and pressure gradients, vapour volume fractions and turbulence quantities etc. are critically analysed and discussed. Orifice thickness was found to significantly influence cavitation behaviour, with the pressure ratio required to initiate cavitation found to vary by a factor of 10 for orifice thickness to diameter (l/d) ratios in the range of 0 – 5. Inlet radius similarly has a pronounced effect on cavitational activity. The results offer useful guidance to the designer of HC devices, identifying key parameters that can be manipulated to achieve the desired level of cavitational activity at optimised hydrodynamic efficiencies. The models can be used to simulate detailed time-pressure histories for individual vapour cavities, including turbulent fluctuations. This in turn can be used to simulate cavity collapse and overall performance of HC device. The presented approach and results offer a useful means to compare and evaluate different cavitation device designs and operating parameters.

Key words: Hydrodynamic cavitation, orifice, CFD, multiphase, turbulent, design

1 Introduction

Controlled hydrodynamic cavitation (HC) is a topic of increasing interest in reactor engineering, offering an attractive potential route to process intensification for a diverse range of industrial applications. For wastewater in particular, HC could potentially play a critical role in future treatment strategies (Ranade and Bhandari [1]). Numerous bench scale studies have highlighted the promise of HC to treat a range of pollutants, including organics [2,3], pharmaceutical compounds [4,5] and common fertilizers and pesticides [6–8]. HC has also been studied as a potential mechanism to inactivate micro-organisms such as E-coli [9]. In production processes, examples of the successful use of HC have been reported for applications ranging from bio-diesel synthesis [10,11], bio-mass pre-treatment [12,13], nano-emulsion production [14], through to fine particle separation [15]. The reported experimental studies typically employ non-optimised operating conditions and HC devices however, typically of orifice plate or venturi construction, and the role that the numerous interacting design & process parameters play in overall reactor performance is not yet fully understood. These factors include the liquid phase properties, operating temperatures and pressures, the structure & concentration of the contaminant (or product), the device geometry, and importantly the nature of the generated cavitation behaviour itself in terms of inception, bubble growth and final collapse.

Orifice is one of the most widely used devices for hydrodynamic cavitation. Despite wide spread use, the role and interactions among various design and operating parameters on the resulting cavitation behaviour is not yet adequately understood. In this work we focus on computational investigations of cavitation in various orifice designs over range of operating conditions. Some studies have indicated the strong influence that orifice geometry has on overall performance; Arrojo et al. [9] reported a parametric study of E-coli disinfection using a series of venturi and orifice type reactor designs. Three orifice deigns were studied featuring various combinations of hole number and diameter, designed to give the same area ratio. The difference in inactivation rates between the worst and best performing devices was found to be a factor of 15. Vichare [16] compared the performance of orifice plates having a range of hole numbers and diameters by measuring the iodine liberated from potassium iodide by HC, and found a factor of 3 difference between the best and worst performing devices. The disparate range of geometries, target compounds and operating conditions in the open literature makes it generally difficult to draw firm conclusions on reactor design. In particular, a detailed understanding of the factors governing the inception and evolution of cavitation is a required starting point, providing a basis to judge differences in degradation performance based on a fundamental description of physical flow features, such as turbulence properties, pressure recovery rates and the inception and extent of cavitation.

Orifice type devices are extensively used in pressurized fluid handling systems, and the influence of geometry on both cavitating and non-cavitating flow behaviour has been the subject of numerous studies. In fuel injection systems for example, the orifice geometry plays a crucial role in the stability and uniformity of spray generated as fuel is forced through the restriction, and ultimately therefore on the emissions produced. Pearce & Lichtarowicz [17] presented experimental studies of the influence of geometry on the discharge coefficient, C_d, for a range of submerged long orifice designs under both cavitating & non-cavitating conditions. Without cavitation, at Reynolds numbers of the order of 10,000 the discharge coefficient was found to remain constant for any given orifice. At these Reynolds numbers, they presented the following correlation for C_d with length to diameter ratio (l/d):

$$(C_d)_{max} = 0.827 - 0.0085(l/d) \quad (1)$$

This results in a decrease in discharge coefficient with increasing l/d ratio, however it should be noted that this study considered only long or deep orifice designs ($l/d > 2$). Under cavitating conditions, an alternative equation was presented which gives the discharge coefficient as a function of a cavitation parameter, K:

$$C_d = C_c\sqrt{1+K} \quad (2)$$

Where C_c is the contraction coefficient (determined experimentally from [17] to be equal to 0.61 for a sharp-edged inlet), and the definition of the cavitation parameter, K, is given in Eq. (3):

$$K = \frac{p_2 - p_v}{p_1 - p_2} \quad (3)$$

In Eq. (3), p_2 denotes the downstream, or fully recovered pressure, p_v is the saturated vapour pressure of the medium, and p_1 is the upstream driving pressure. The definition in Equation (2) therefore describes a decreasing discharge coefficient with increasing pressure ratio, which tends to a minimum value equal to the value of C_c. The authors also reported that the pressure ratio required for cavitation inception tended to increase with increasing *l/d* ratio.

Nurick [18] presented a comprehensive study of a range of orifice designs having varying *l/d* ratio, as well as different orifice inlet conditions. In the cavitating regime, Nurick proposed an alternative expression for C_d:

$$C_d = C_c \sqrt{\frac{p_1 - p_v}{p_1 - p_2}} \quad (4)$$

Where:

$$C_c = 0.62 + 0.38(A_1/A_0)^3 \quad (5)$$

A_1 is the area of the upstream pipe, or plenum, and A_0 is the area of the orifice restriction. Note that the relationships presented in Equations (2) & (4) are equivalent if a common value of C_c is imposed; the difference is therefore simply down to the higher values of C_c produced by Equation (5), which results in higher overall calculated discharge coefficients. Nurick additionally observed that the orifice inlet conditions had a significant effect on discharge coefficient and cavitation inception; experimental measurements revealed the critical pressure ratio required to initiate observable cavitation increased linearly with inlet roundness, and suggested the following relationship for the critical cavitation number, K_{cr}:

$$K_{cr} = \frac{p_1 - p_v}{p_1 - p_2} = -11.4(r/d) + 2.6 \quad (6)$$

More recently Ohrn et al. [19] reported measured C_d values with varying *l/d* ratio, and found good agreement with the work presented in [17] & [18]. They reported no appreciable influence on C_d with increasing *l/d* ratios above 2 for sharp edged nozzles, however inlet rounding was again found to have a significant effect. Measured discharge coefficients were found to increase from values around 0.68 at *r/d* ratios of 0.05 up to 0.98 at *r/d* ratios of 0.5. Ramamurthi et al. [20] also presented measurements of orifice atomisers with *l/d* ratios varying from 1 to 50, and also observed that cavitation inception was progressively delayed as aspect ratios increased beyond values of 5.

Despite these results on influence of *l/d* and sharpness of orifice on realised cavitation, many studies reporting use of hydrodynamic cavitation for variety of application focus only on free area and perimeter of orifice holes (see a recent review by Carpenter [21], Arrojo et al. [9]) and do not report these parameters. Many of the HC application studies use relatively shorter orifices with *l/d* ratios typically less than 2. For example, Braeutigam et al. [22] studied a total of 25 orifice plates with thickness of 2mm thick orifice plates in order to determine the effect of area ratio on the decomposition of chloroform in water. Out of this series of 25 configurations all had *l/d* ratios of 2 or lower except one. The performance of such shorter orifices on the realised cavitation is not adequately studied, and the correlations discussed earlier are not applicable for such shorter orifices as they are all derived from empirical data for long orifices, with *l/d* ratios greater than 2. Besides the sharpness of orifices, the angle made by the hole with the centreline is also one of the key parameters affecting the inception and extent of cavitation. Adequate information and understanding of these factors is lacking and therefore resulted in significant gaps in design and optimisation of a relatively simple cavitation devices like orifices. In this work we have attempted to fill some of these gaps.

At this point it should be mentioned that the expressions given in Eq.(3) & Eq.(6) are just two in a large number of definitions of cavitation parameter, or cavitation number. Differences can be found across the published literature in the pressure terms and averaged velocity terms used as the basis for reported cavitation numbers.

A comprehensive discussion of the issues surrounding inconsistent reporting of cavitation number can be found in [23]. For the duration of this study, unless explicitly stated otherwise for the purposes of comparison with published experimental values, the definition of cavitation number, c_a, is as follows:

$$c_a = \frac{p_2 - p_v}{{}^1/_2 \rho_l u_t^2} \tag{7}$$

Where ρ_l is the liquid phase density, and u_t is the velocity at the orifice throat. Eq.7 provides a simple means of estimating the potential for cavitation to occur; observable cavitation will first initiate at some particular value of c_a, known as the incipient cavitation number, or cavitation inception number c_{ai}. Typically this occurs at values close to 1, where the dynamic pressure is equal to the difference in recovered pressure p_2 and the vapour pressure p_v. As the value of c_a further decreases, the number and size of vapour cavities increases. A number of factors influence the cavitation inception process; for cavitation to initiate the presence of nuclei is required in the form of small gas bubbles. The number and size distribution of these nuclei influences the point at which inception occurs. For example, in some cases, when the nuclei present are relatively small and few in number the liquid can withstand pressures lower than the vapour pressure before cavitation occurs. In lieu of quantitative information on bubble nuclei it is necessary to make some simplifying assumptions. In this work, it is assumed that the quantity and initial sizes of gas nuclei are such that cavitation inception is determined solely as a function of the minimum predicted static pressures within each device relative to the liquid vapour pressure. Additionally, the effect of gases coming out of solution above the vapour pressure is not considered within the scope of this investigation. In this way we can compare the influence of different geometrical configurations on cavitation inception on a consistent basis, and importantly determine the energy input required to initiate and drive the cavitation process.

In this study we develop and use multiphase computational fluid dynamics (CFD) models for simulating cavitating flow through orifice, and compare the results to experimental data available in open literature. In order to predict cavitation behaviour suitable mass transfer models are adopted to describe the formation and growth of water vapour within pure liquid water at an ambient temperature of 22°C. A full description of the modelling approach is presented in Section 2. Throughout this paper an Eulerian-Eulerian approach is adopted to calculate cavitation mass transfer, with supplementary Lagrangian calculations then performed using the solved Eulerian flow fields to extract information on individual bubble trajectories. The predicted results in terms of velocity and pressure gradients, vapour volume fractions and turbulence quantities etc. are critically analysed and discussed. The baseline orifice design used in this investigation is shown in Figure 1a; a simple, cylindrical sharp edge orifice with d/D = 0.22 and l/d= 2. The influence of orifice l/d ratio and inlet conditions are investigated by studying a series of parametrically varying designs (Figure 1b). The model equations and numerical solution are discussed in the following section. As each configuration studied in this work is cylindrical, 2D axis-symmetric simulations are performed throughout. The simulated results are discussed in Section 3, and offer useful guidance to the designer of hydrodynamic cavitation devices, identifying key geometric parameters that can be manipulated to achieve the desired level of cavitational activity at optimised hydrodynamic efficiencies. The models and simulated flow field can be used to simulate detailed time-pressure histories for individual vapour cavities, including turbulent fluctuations. This in turn can be used to simulate cavity collapse and overall performance of hydrodynamic cavitation device. The presented approach and results offer a useful means to compare and to evaluate different designs of cavitation devices and operating parameters.

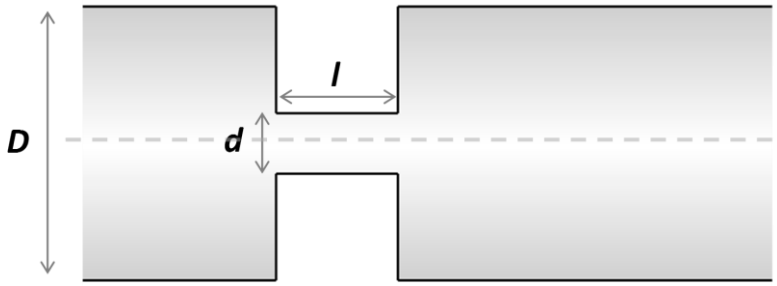

Figure 1a: Baseline Orifice Geometr

Parameter	Figure (Axis-symmetric)	Range
Thickness of orifice plate (l/d)	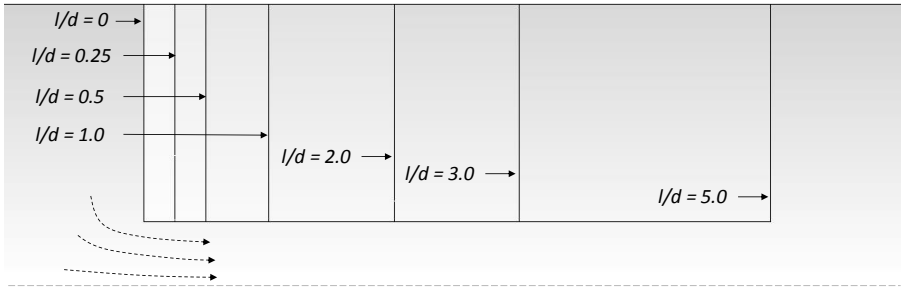	l/d = 0, 0.25, 0.50, 1.0, 2.0, 3.0, 5.0
Radius of curvature at the inlet of orifice	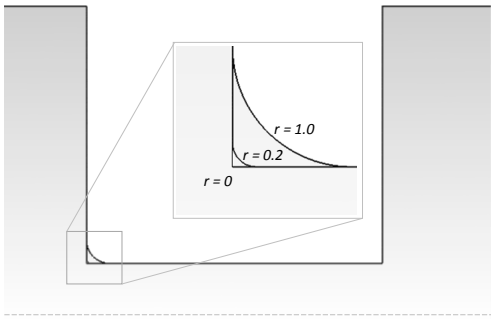	r/d = 0.0, 0.03, 0.16
Angle of orifice hole	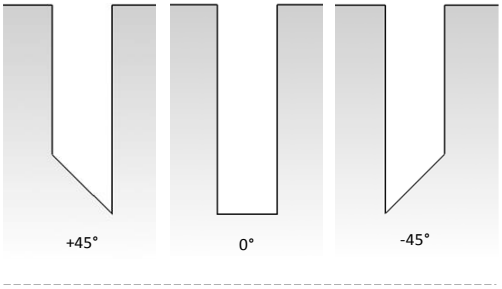	θ= +45°, 0°, -45°

Figure 1b: Orifice designs with varying l/d ratio, inlet radii & hole angle

2 Mathematical models

In an orifice or similar flow restriction, cavitation occurs when the flow rate attained is sufficient to drive local pressures within the throat of the device down to the saturated vapour pressure of the liquid. Cavitation inception is marked by an initial transition from a single-phase flow to a two phase bubbly flow, and as flow rate increases an increasingly complex flow field develops. Flow fields are typically highly turbulent; larger gas filled vapour structures form, grow, and trigger vortex breakup. Discrete cavities can undergo oscillatory growth, coalescence and break up before finally collapsing as they are transported into higher pressure regions. The spatial and temporal timescales over which these events occur span a wide range, and as such modelling cavitation is a particularly complex task. The most fundamental approach is to apply Direct Numerical Simulation (DNS), which resolves the smallest scales of turbulence and cavity evolution. However the extreme computational demands limit this approach to the study of relatively small fluid volumes and bubble quantities [24]. Considering that the focus of this work is on carrying out large number of simulations for a wide range of design and operating parameters, we used RANS (Reynolds averaged Navier-Stokes) approach with appropriate turbulence model. A pseudo homogeneous or a mixture model, in which the working medium is treated as a single fluid composed of a homogenous mixture of two phases, is used with appropriate relationships defined to drive mass transfer. The following sections (2.1 and 2.2) describe the model equations representing the cavitating two-phase flow field with phase change. Besides obtaining the time averaged flow field, it is useful to simulate transient trajectories of cavities within the flow domain to gain insight about the time-pressure histories experienced by cavities as they are transported through the device. To achieve this, the Eulerian mixture computations were coupled to the Lagrangian simulations for discrete cavity trajectories. The model equations for these Lagrangian simulations are discussed in Section 2.3.

2.1 Flow & turbulence models

The working medium is treated as a single fluid, comprised of a homogeneous mixture of two phases. The continuity equation for the mixture flow is written as:

$$\frac{\partial}{\partial t}(\rho_m) + \nabla \cdot (\rho_m \vec{u}_m) = 0 \tag{8}$$

Where ρ_m is the mixture density, & $\vec{u}_m$ is the mass-averaged mixture velocity. The corresponding momentum equation for the mixture flow, assuming that both phases share the same velocity field, is written as:

$$\frac{\partial}{\partial t}\left(\rho_m \vec{u}_m\right) + \nabla \cdot \left(\rho_m \vec{u}_m \vec{u}_m\right) = -\nabla p + \nabla \cdot \left[\mu_m\left(\nabla \vec{u}_m + \nabla \vec{u}_m^T\right)\right] + \rho_m \vec{g} + \vec{F} \tag{9}$$

Where $\vec{u}_m$ is the mixture velocity vector, μ_m is the mixture viscosity, $\rho_m \vec{g}$ is the gravitational body force, and the term $\vec{F}$ accounts for additional external body forces applied to the fluid volume (i.e. that may arise from interaction with dispersed phases). In Reynolds averaged (RANS) approaches, the velocity terms in Equations (8) & (9) are replaced by the sum of their mean ($\bar{u}$) and instantaneous (u') components, $u = \bar{u} + u'$, and an ensemble average taken. This averaging process results in additional terms representing the effects of turbulence. These additional terms take the general form $\partial/\partial x_j\left(-\rho\overline{u_i u_j}\right)$, and are known as the Reynolds stresses. In order to close the momentum equation, the introduced Reynolds stress terms require additional mathematical models. One approach is to use a Reynolds Stress Model (RSM), which involves solving separate transport equations for each of the additional Reynolds stresses (6 in total for 3D cases). More typical in RANS approaches is to employ the Boussinesq hypothesis, which approximately relates the Reynolds stresses to the mean velocity gradients in the flow as follows:

$$-\rho\overline{u_i u_j} = \mu_t\left(\frac{\partial u_i}{\partial j} + \frac{\partial u_j}{\partial i}\right) - \frac{2}{3}\rho k \delta_{ij} \tag{10}$$

Here the subscripts *i* & *j* represent two mutually perpendicular directions, *k* is the turbulent kinetic energy, and δ_{ij} is the Kronecker delta, which is introduced to make the formula applicable to the normal stresses where i = j Most importantly, this expression also introduces the concept of the turbulent viscosity, μ_t. This is not a physical property, but rather a scalar which has a value proportional to the local turbulence properties. This quantity is typically modelled through additional transport equations for the turbulent kinetic energy (*k*) and turbulent dissipation rate (ε), or the specific dissipation rate (ω). The choice of turbulence closure model is crucially important, particularly so in cavitating regimes. The flow fields encountered in this investigation feature flow separation & reattachment, large density gradients, the formation of jets & shear layers and adverse pressure gradients. Following a comparison of different closure models, including an *RSM* model, the Shear Stress Transport (*SST) k-ω* model of Menter [25] has been selected for use throughout this study, which has been found in previous studies to demonstrate superior predictions to other 2-equation approaches in situations involving flow separation and adverse pressure gradients (see for example Bardina et al. [26]. The rationale for selecting this turbulence model is further discussed later in Section 3.2 while discussing the results from different turbulence models. The turbulent viscosity, μ_t in the *SST k-ω* model is defined as:

$$\mu_t = \frac{\rho k}{\omega} \tag{11}$$

The transport equations for *k* & ω are then written as follows:

$$\frac{\partial}{\partial t}(\rho k) + \frac{\partial}{\partial x_i}(\rho k u_i) = \frac{\partial}{\partial x_j}\left(\Gamma_k \frac{\partial k}{\partial x_j}\right) + G_k - Y_k + S_k \tag{12}$$

and:

$$\frac{\partial}{\partial t}(\rho \omega) + \frac{\partial}{\partial x_i}(\rho \omega u_i) = \frac{\partial}{\partial x_j}\left(\Gamma_\omega \frac{\partial \omega}{\partial x_j}\right) + G_\omega - Y_\omega + S_\omega \tag{13}$$

G represents the generation, Γ the effective diffusivity, and *Y* is the dissipation due to turbulence [27]. The subscripts *k* and *w* denote turbulence production and dissipation respectively. S_k & S_w are user-defined source terms.

2.2 Cavitation model

Various mass transfer models have been proposed to describe the cavitation process, with the most commonly used approaches based on reduced forms of the Rayleigh-Plesset equation. Examples include the models proposed by Schnerr & Sauer [28], Zwart et al. [29] and Singhal et al. [30]. The computational work described in this paper is based on the latter cavitation model developed by Singhal; this has been validated against a wide range of flow cases (see examples in [30], [31]), and offers the advantage that the bubble number per unit volume, *n*, need not be prescribed as input. In this model, the vapour volume fraction is computed locally from a transport equation for the vapour mass fraction, *f*, (14), which introduces an additional pair of mass source and sink terms for the evaporation (R_e) and condensation (R_c) of the vapour:

$$\frac{\partial}{\partial t}\left(\rho_m f\right) + \nabla \cdot \left(\rho_m \vec{v}_m f\right) = \nabla \cdot \left(\Gamma \nabla f\right) + R_e - R_c \tag{14}$$

Where:

$$\frac{1}{\rho_m} = \frac{f}{\rho_v} + \frac{1-f}{\rho_l} \tag{15}$$

Here ρ_m, ρ_v and ρ_l refer to the densities of the mixture, vapor and liquid respectively. The vapor volume fraction, α, can then be calculated as follows:

$$\alpha = f\frac{\rho_m}{\rho_v} \tag{16}$$

In the Singhal approach [30], the evaporation and condensation terms are derived from a reduced form of the Rayleigh-Plesset equation, commonly shortened to the R-P equation [32]:

$$\rho\left[R_B\frac{d^2R_B}{dt^2} + \frac{3}{2}\left(\frac{dR_B}{dt}\right)^2\right] = p_B - p - \frac{2\sigma}{R_B} - \frac{4\mu}{R_B}\frac{dR_B}{dt} \tag{17}$$

In this expression, R_B *is the bubble radius,* p_B refers to bubble surface pressure, and *p* is the local liquid phase pressure. Full derivation of the R-P equation is presented in [32], and numerous examples of solutions of the R-P equation exist in literature, for example Alehossein & Qin [33]. Commonly, when modelling cavitation mass transfer mechanisms in CFD codes, the R-P equation for bubble growth is used to approximate void propagation. To derive mass transfer terms compatible with the Eulerian-Eulerian multiphase approach, the surface tension, viscous damping and higher order acceleration terms in Eq.(17) are neglected to produce a mass transfer rate term of the following form:

$$\frac{dR_B}{dt} \cong (-1)^n\sqrt{\frac{2}{3}\frac{(p_B - p)}{\rho_l}} \tag{18}$$

Where n=1 during bubble expansion / evaporation, and n=2 during the condensation phase. Using this approach, Singhal et al. [30] derived a simplified vapour transport equation:

$$\frac{\partial}{\partial t}\left(\rho_m f\right) + \nabla \cdot \left(\rho_m \vec{v}_m f\right) = (n4\pi)^{1/3} + (3\alpha)^{1/3}\frac{\rho_v\rho_l}{\rho}\left[\frac{2}{3}\left(\frac{p_B - p}{\rho_l}\right)\right]^{1/2} \tag{19}$$

Equation (19) is referred to as the *Reduced Bubble Dynamics Formulation*. All terms in this expression except n, the bubble number density, are either known constants or dependent variables. To avoid having to specify a bubble number density, the phase change expression is rewritten in terms of bubble radius

$$R_e = \frac{3\alpha}{R_B}\frac{\rho_v \rho_l}{\rho_m}\left[\frac{2}{3}\left(\frac{p_B - p}{\rho_l}\right)\right]^{1/2} \tag{20}$$

The typical bubble size, R_B, is taken to be equal to the limiting (maximum possible) bubble size using a correlation commonly used in the nuclear industry:

$$R_B = \frac{0.061 We \sigma}{2\rho_l u_{rel}^2} \tag{21}$$

Where *We* is the Weber number, and σ is the surface tension; Weber number is given by the following expression:

$$We = \frac{\rho_l u_l R_B}{\sigma} \tag{22}$$

In which ρ_l and u_l are the liquid density and velocity respectively. In the Singhal model, the square of the relative velocity term is approximated as a linear characteristic velocity, $u_{rel}^2 = u_{ch} = \sqrt{k}$ (In bubbly flows the phase change rate is proportional to u_{rel}^2, however most practical two-phase flow regimes display a linear dependence). The relative velocities and turbulent velocity fluctuations are of the same order (1-10%), and as such $\sqrt{k}$ is considered to be a suitable approximation for u_{ch}. This produces the following final pair of phase change rate terms:

$$R_e = C_1 \frac{\max(1.0, \sqrt{k})}{\sigma} \rho_v \rho_l \left[\frac{2}{3}\left(\frac{p - p_v}{\rho_l}\right)\right]^{1/2} (1 - f_v - f_g) \tag{23}$$

$$R_c = C_2 \frac{\max(1.0, \sqrt{k})}{\sigma} \rho_v \rho_l \left[\frac{2}{3}\left(\frac{p - p_v}{\rho_l}\right)\right]^{1/2} f_v \tag{24}$$

Here C_1 and C_2 are empirical constants, for which Singhal et al. [30] recommend values of 0.2 and 0.01 respectively following their extensive studies on a range of sharp edged orifice & hydrofoil flows. Additionally, in order to take account of the effect of the magnitude of local turbulent pressure fluctuations (p'_{turb}), a modified term for the local saturated vapour pressure, p'_v is calculated as a function of the local turbulent kinetic energy, *k*, and the liquid saturated vapour pressure, p_v, as given by the following relationships:

$$p'_{turb} = 0.39 \rho_m k \tag{25}$$

$$p'_v = p_v + p'_{turb}/2 \tag{26}$$

Where ρ_m is the mixture density, *k* is the turbulent kinetic energy, and the constant value of 0.39 is taken from [30].

2.3 Lagrangian discrete phase model (dpm)

Trajectories of individual cavities were simulated using the Lagrangian approach. Since the two-phase flow field is already computed using the models described above, one-way coupling was assumed between the discrete cavities and the continuous mixture while simulating cavity trajectories. The cavity trajectories are driven by the primary flow gradients and turbulence quantities. The particle trajectories are computed by integrating the force balance for a discrete particle of a series of discrete time steps; the force balance is given as:

$$\frac{d\vec{u}_p}{dx} = \frac{\vec{u} - \vec{u}_p}{\tau_r} + \frac{\vec{g}(\rho_p - \rho)}{\rho_p} + \vec{F} \tag{27}$$

This equates the particle inertia with the forces acting on the particle. The first term on the right-hand side of the equation is the drag force per unit mass of the particle, and the second term is the force due to gravity. The final term, $\vec{F}$, is an additional acceleration term, through which additional force terms can be incorporated into the overall balance to account for phenomena such as virtual mass, pressure gradient forces and particle rotation. The influence of continuous phase turbulence on the tracked particles can be accounted for by separating the velocity, *u,* into the sum of the mean and instantaneous components:

$$u = \bar{u} + u' \tag{28}$$

In the work presented here, the discrete random walk model, or "eddy lifetime" model is used to include the effects of turbulence on the discrete cavity trajectories [27]. In this approach, each discrete particle is considered to interact with a succession of discrete turbulent eddies which modify their instantaneous velocities. This involves introducing two modelled terms; firstly, the random fluctuating component of velocity is calculated as a function of the local turbulent kinetic energy value:

$$u' = \zeta\sqrt{2k/3} \tag{29}$$

Where ζ is a normally distributed random number. Secondly, the concept of a particle eddy lifetime, T_L, is introduced to define the time intervals over which this random fluctuating component is updated. This "eddy lifetime" is approximated as a function of the local turbulence frequency:

$$T_L \approx 0.15\frac{k}{\varepsilon} \tag{30}$$

Additional limits can be placed on the maximum time step size; in this study a minimum of 5 time steps is also imposed across any given computational cell.

Using the solved Eulerian flow field, discrete cavities were initialised on an iso-surface of volume fraction equal to 1; the edge of the predicted vapour filled cavity. The particles were considered to be massless, and therefore act as flow followers. A large number of trajectories were computed, and from these a sample were selected (10), and the time histories of pressures & turbulence quantities experienced by the cavities collected, averaged and analysed.

3 Results & discussion

3.1 Numerics and convergence strategy

The model equations described in the preceding section were all solved using commercial CFD code, Ansys Fluent (v17). Throughout this work 2D axis-symmetric calculations were performed. In each case the pressure ratio was fixed by inlet and outlet pressure boundary conditions, making the flow-rate solution dependent.

Initially single-phase calculations were carried out, and the cavitation model was then subsequently activated using the solved single-phase results as initial conditions. With the cavitation model enabled, at higher Reynolds numbers it was necessary to switch to unsteady RANS in order to obtain convergence ($1x10^{-5}$ in all RMS residuals), using a timestep size of 1e-5s. Although in this study no large scale unsteady structures or fluctuations in the predicted flow rates were observed across the investigated range; at higher Reynolds numbers, a small region of fluctuation was observed restricted to a small area around the exit edge of the orifice. The SIMPLE algorithm was used for pressure velocity coupling, with 2^{nd} order discretization applied to the momentum, pressure and turbulent quantities in each instance. For vapor transport, a first order scheme was used to ensure convergence.

To determine the sensitivity to grid refinement, particularly local cell sizes and growth ratios in the orifice throat, a series of 6 successively refined meshes were investigated. Grid sizes of 16,000 cells; 26,000; 60,000; 120,000; 225,000 as well as a final grid of 450,000 cells were constructed and converged results obtained from each. The grid sizes of 16,000 and 26,000 cells had target y+ values in the 10-30 range suitable for a log-law approximation, whereas grid sizes from 60,000 and above featured boundary layer resolution down to the viscous sub-layer. The variation in predicted wall y^+ for a selection of the grids studied, and the variation in predicted flow rates with increasing grid size are shown in the supplementary information, along with detailed comparisons of the axial velocity and turbulence kinetic energy profiles (Figure SI.1, Figure SI.2 & Figure SI.3 respectively). A cell count of 120,000 with resolved wall boundary layers was found to be necessary to obtain adequate mesh convergence. For the subsequent parametric study, the same mesh settings were translated onto the different geometries such that the same refinement levels were maintained in the x- and y- directions.

3.2 Turbulence closure model sensitivity

To assess the influence of the choice of turbulence model, results of predicted flow and turbulence quantities were compared at the orifice throat using four different closure models; the standard *k-ε*, renormalized group *k-ε*, *k-ω SST* and an *ω*-based *RSM* model. The predicted velocities and turbulent kinetic energy at the vena contracta, shown in Figure 2, demonstrate negligible difference between the *RSM* model and *k-ω SST* model predictions. The *RNG k-ε* model shows a similar distribution of turbulent kinetic energy, with a slightly higher free-stream value away from the wall. The difference in predictions with the standard *k-ε* based models is pronounced however; the detailed of the separation region and reversed flow at orifice entry are not repeated, and predicted turbulent kinetic energy is significantly higher across the cross section. In terms of overall predicted flow rate, there is less than 1.5% deviation between the *k-ω SST*, *RSM* and *k-ε RNG* models, whereas the flow rate predicted by the standard *k-ε* model is 5% lower.

Relative to the *k-ω SST* model the *RSM* model incurs a higher computational overhead, and this consistency in predictions, in the absence of further validation of these predicted quantities, was considered justification to adopt the *k-ω SST* for use in the remainder of the study. Additionally this model has been shown to offer improved accuracy in a number of comprehensive validation studies of complex flow cases involving separation and adverse pressure gradients [26]. The *k-ω SST* model overcomes deficiencies in the standard *k-ω* and *k-ε* models by introducing blending functions, which switch from a *k-ε* model in the bulk of the flow domain to a *k-ω* model in near wall regions. The *k-ω* model is generally accepted to be more accurate and robust in near wall regions, owing to the existence of an analytical expression for *ω* in the viscous sub region of the boundary layer, whereas *ε* based models rely on the specification of damping functions to ensure that the viscous stresses dominate over the turbulent stresses in the viscous sub layer. An added advantage of the *k-ω SST* model is the use of automatic wall functions, which switch between a fully resolved boundary layer calculation and a log-law approximation depending on the local near wall grid refinement.

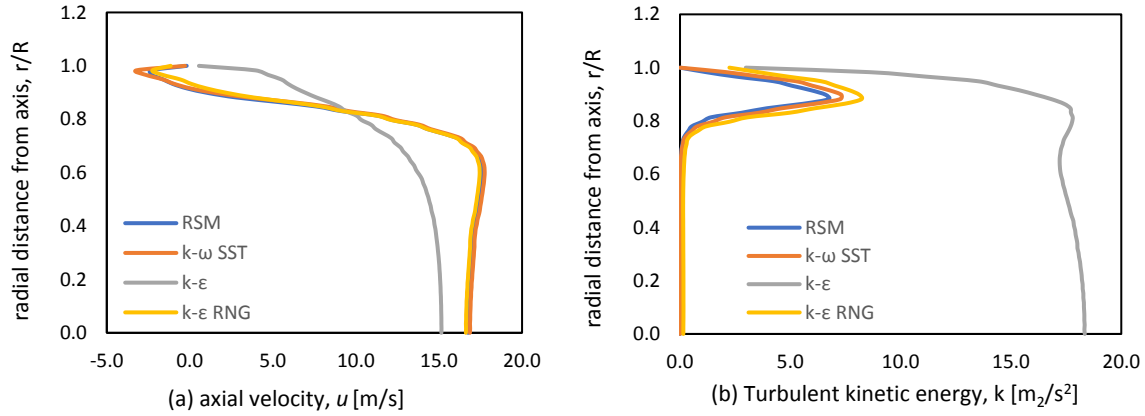

Figure 2: axial velocity (a) and turbulent kinetic energy (b) profiles at the vena contracta for different turbulence closure models

3.3 Comparison with the experimental data of Ebrihimi et al. [30]

The orifice geometry selected for comparison is based on the dimensions used by Ebrihimi et al. [31], for which a large dataset is available for cavitating flow under high flow rates and operating pressures. Figure 3 presents a comparison of predicted flow rate versus operating pressure ratio against the experimental data published in [31]. Calculations were performed at 3x different inlet pressures, ranging from 300 – 2000 Psi. The multi-phase CFD results show good agreement with the experimental measurements across the considered operating range; for the 2000 Psi cases, the single-phase predictions are also plotted for comparison. The cavitation model is shown to successfully reproduce the transition to choked flow as cavitation initiates and evolves. Cavitation inception number, c_{ai}, was predicted to be equal to 1.46 for the 2000 Psi case.

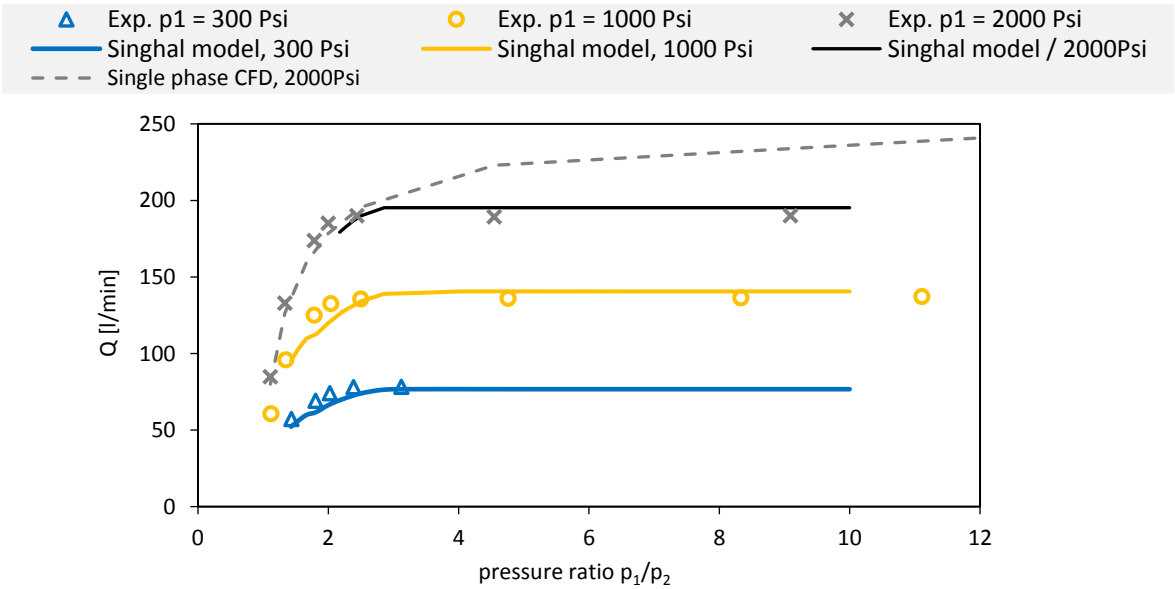

Figure 3: Flow rate v pressure ratio (experimental data from Ebrahimi et al. [31])

3.4 Influence of device pressure ratio

As the inlet to outlet pressure ratio increases, flow through orifice increases and lowest pressure occurring within the system starts decreasing. The simulated pressure profiles along both the outer orifice wall and the central axis are shown in Figure 4a for a series of increasing pressure ratios. Initially at a Pr of 2.0 a low pressure region is formed as the flow separates at orifice entry, which then grows radially inwards towards the centreline as pressure ratio is increased. Cavitation inception occurs when this local low pressure region formed due to separation approaches the vapour pressure. Figure 4b illustrates the pressure field in the orifice throat at the

predicted cavitation inception point (Pr = 2.5, 2000 Psi inlet), and the evolution of the pressure field is illustrated in Figure 4c which shows contours at an overall Pr of 3.3. As pressure ratio increases, the low pressure region along the outer wall continues to grow, until at a pressure ratio of 5 the outer walls of the orifice restriction are equal to the vapour pressure along the full length of the orifice. At pressure ratios of 5 and above, the absolute pressure along the centreline also reaches the saturated vapour pressure. This corresponds to a cavitation number, c_a equal to 0.3. The corresponding vapour volume fractions are plotted in Figure 4d, clearly showing the evolution of the vapour cavity along the outer surfaces of the orifice throat. Inception, and the subsequent evolution of the vapour cloud is therefore shown to be governed by the effect of the high total pressure losses incurred as flow accelerates around the sharp-edged orifice.

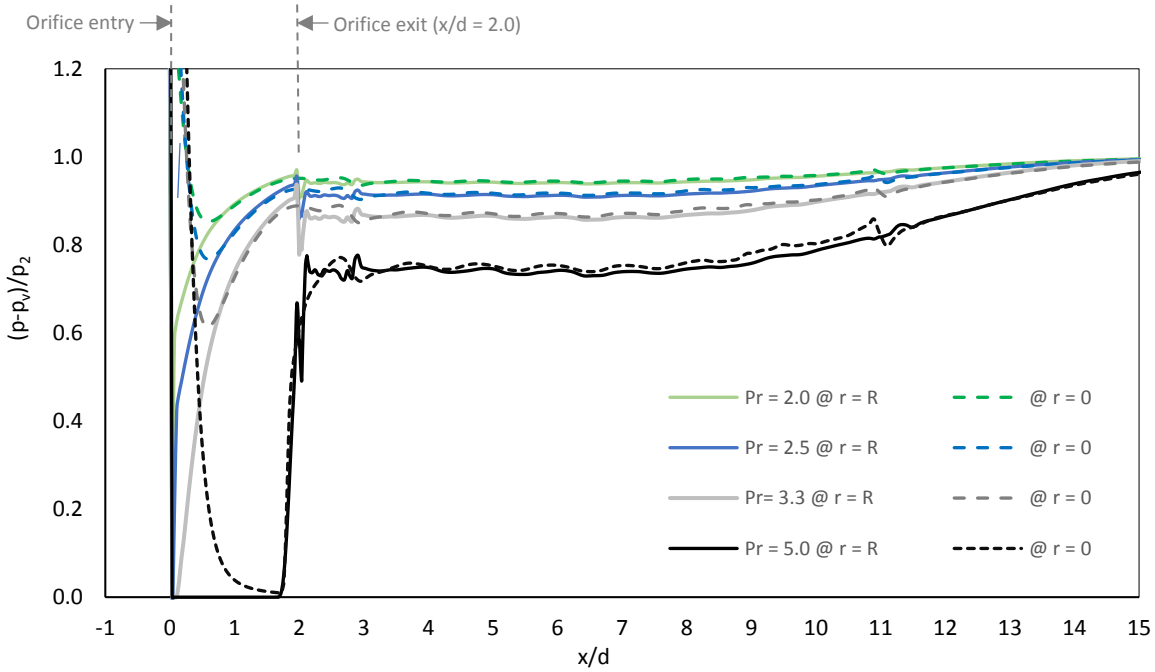

Figure 4a: Pressure distribution v distance

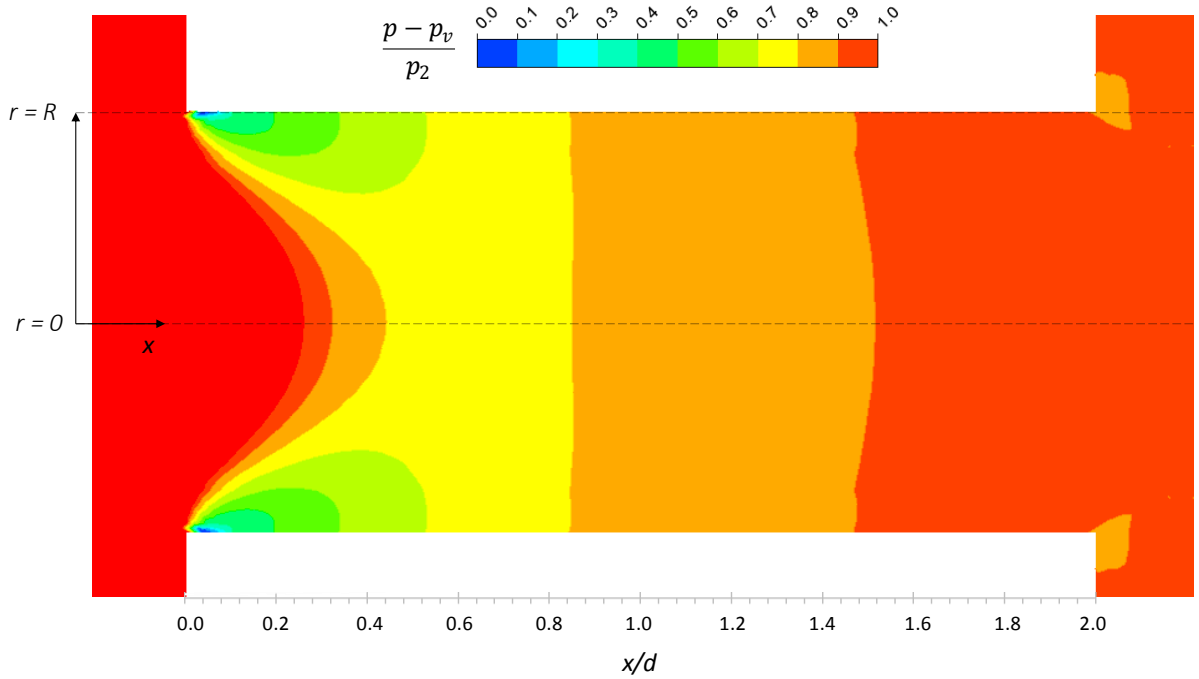

Figure 4b: Pressure in throat at pressure ratio = 2.5, p_1 = 2000 Psi

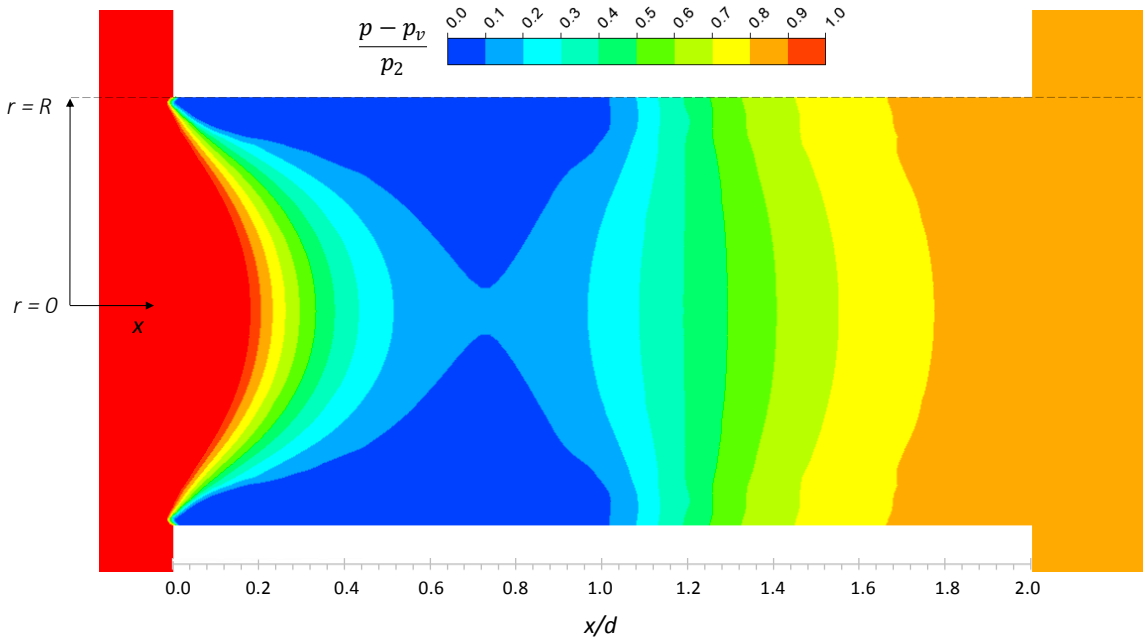

Figure 4c: Pressure in throat at pressure ratio = 3.3, P_1 = 2000 Psi

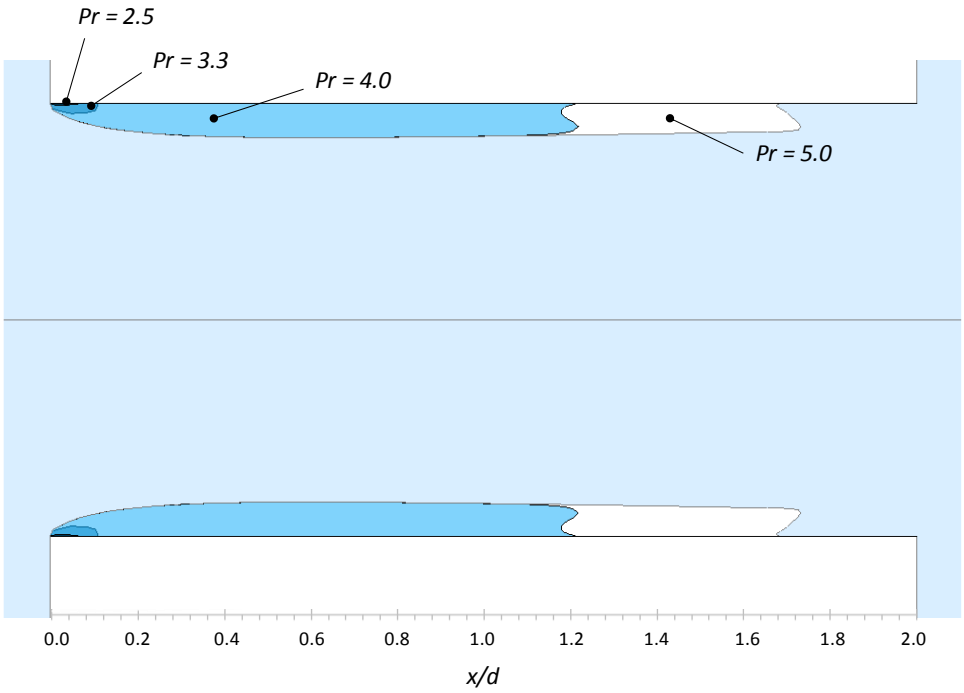

Figure 4d: Contours of constant vapour volume fraction (=0.5) at varying pressure ratios (P1 = 2000Psi)

Figure *4*: Influence of pressure ratio on cavitating flow with orifice

3.5 Influence of orifice thickness (l/d)

The effect of orifice length has been investigated for designs having *l/d* ratios of 0.25, 0.5, 1.0, 2.0, 3.0 & 5.0, as well as a theoretical limiting case of 0.0. As opposed to simulating the high pressure operating conditions used for comparison with published data, the outlet pressure was instead set to atmospheric in each case. For the baseline geometry (*l/d* = 2.0), the cavitation inception number, c_{ai}, is predicted to be 1.5. (This shows negligible difference to the results at elevated operating pressures presented Section 3.3, where c_{ai},=1.46). The

minimum pressure in the orifice throat against pressure ratio for each configuration was examined to identify cavitation inception (see Figure SI.4). Based on this, predicted variation of cavitation inception with l/d ratio is shown in Figure 5a which clearly illustrates the significant influence of this parameter on inception. For the limiting zero length case, large pressure ratios of the order of 20 are required to induce cavitation, corresponding to c_{ai} = 0.13. The required operating pressures for inception show little variation above *l/d* ratios of 2.0, with cavitation inception numbers of the order of 1.5. Although the inception point is consistent, increasing *l/d* ratios beyond 2.0 has the effect of delaying the pressure recovery, and the low-pressure region is maintained through the length of the orifice (see Figure SI.5). Subsequently, the predicted extent of the vapour cavity is shown to increase with increasing *l/d* ratio under matching operating pressure conditions (Figure 5b). The comparison of turbulent kinetic energy for *l/d* ratios of 2 & 5 is shown in Figure SI.6; for the longest orifice, there is a comparatively higher level of turbulent kinetic energy along the length of the outer orifice walls, and subsequently a comparatively lower level in the shear layers beyond the orifice exit.

Predicted discharge coefficient is plotted for each aspect ratio in Figure 5c, suggesting a peak for *l/d* ratios of 2.0 at pressure ratios below 2. Beyond this, as cavitation initiates and the vapour bubble at the inlet forms and grows, there is an initial fluctuation in C_d, before a monotonic decrease is observed. If extrapolated, the C_d value for each *l/d* ratio tends to values of the order of 0.61, which is in good agreement with the trends observed by Pearce and Licharowicz [17]. Plotting their correlation from Eq.(2), using the C_c value of 0.61 stated for a sharp edged inlet in [17], shows good agreement for the cavitating regime, with the trend closely following the curve for an *l/d* ratio of 2.0. Examining the maximum predicted discharge coefficients in the non-cavitating phase, the trends also shows good agreement with experimental trends; Figure 5d shows the maximum C_d values plotted against the correlation from [17] given in Equation (1); the correlation was derived from experimental data for *l/d* ratios of 2 and above, and below these values the results show significant deviation from the linear correlation. The majority of orifice HC reactor studies feature thin orifices of *l/d* <= 2, and as such the correlation suggested in [17] & [18] would appear to be unsuitable at these lower values. Good agreement is however observed above l/d = 2, with the CFD predictions showing a reduction in C_d values.

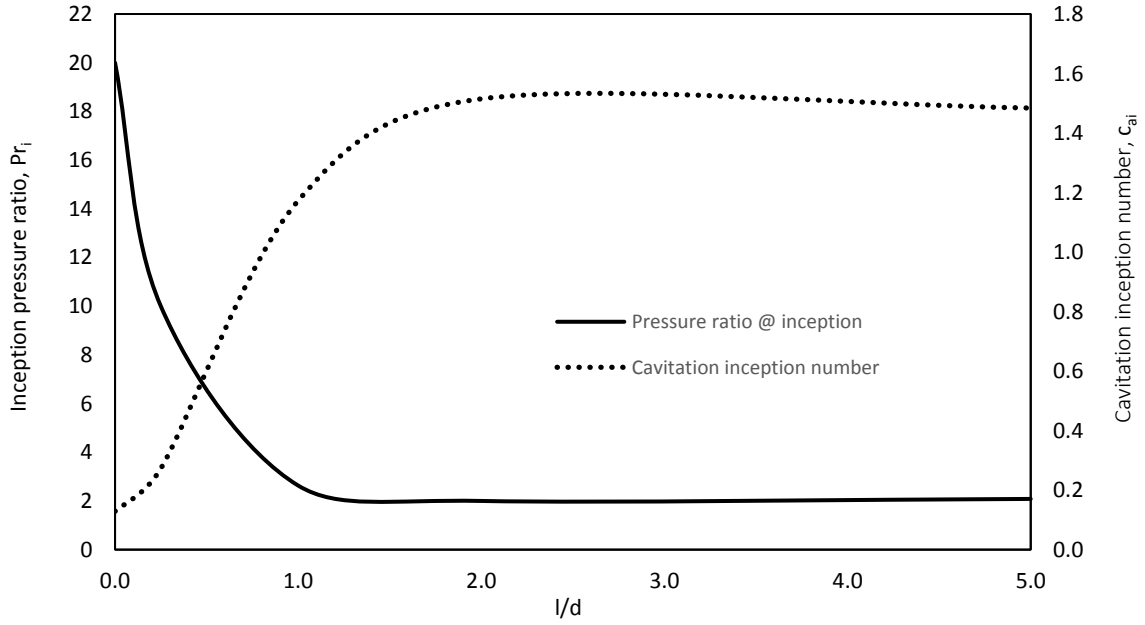

Figure 5a: Cavitation inception number vs aspect ratio

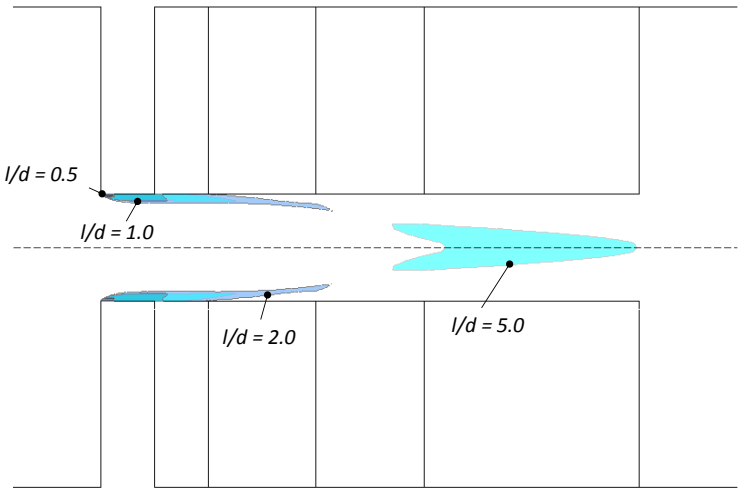

Figure 5b: Contours of constant vapour volume fraction (=0.5) at varying aspect ratios (Pr=5)

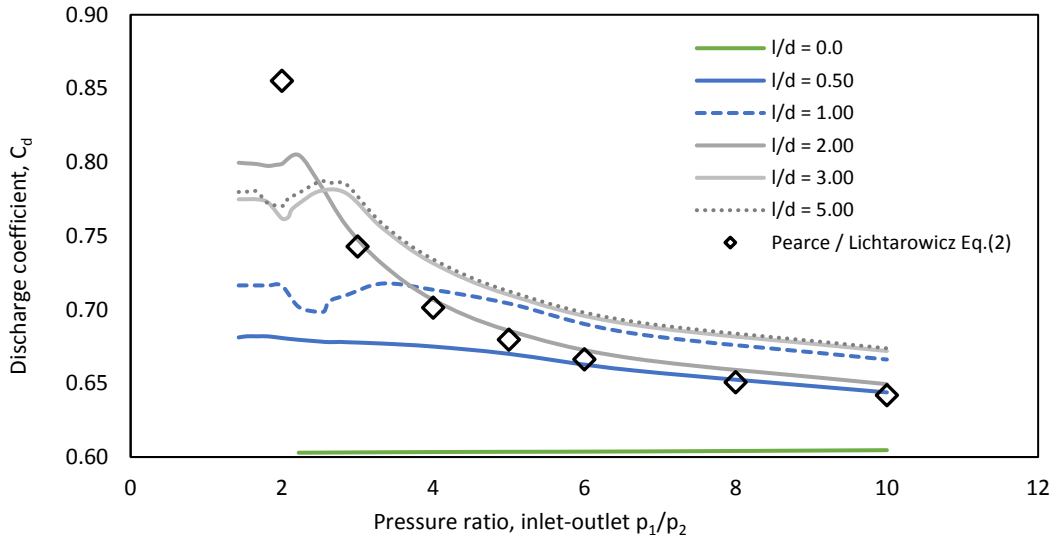

Figure 5c: Discharge coefficient vs pressure ratio for varying aspect ratios

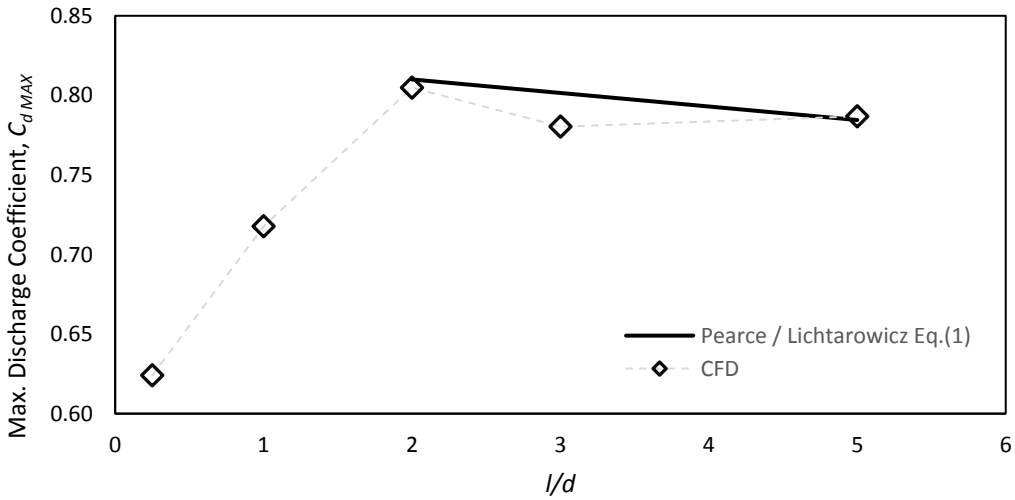

Figure 5d: Maximum discharge coefficient vs l/d ratio for non-cavitating flows

Figure 5: Influence of l/d ratio on cavitating flow with orifice

Using the converged solutions of the Eulerian multiphase flow fields, cavity trajectories were simulated to gain insight into the turbulent pressure fields experienced by the cavities generated at the restriction. In each case, the trajectory calculations were initialized from a surface of constant vapour volume fraction = 1.0, representing the edge of the predicted gas filled cavity in the orifice. For each trajectory, the mean pressures and turbulence quantities were processed, and the fluctuating component of pressure, p', calculated as a function of a normally distributed random number as follows:

$$p' = \bar{p} + \zeta\rho k \tag{31}$$

Discrete cavity trajectories for the baseline case (l/d = 2) are shown in Figure *6*a for the overall device pressure ratio of 5.0. The cavities start their journey from an iso-surface at vapour volume fraction of unity, and from there follow the outer walls of the orifice. Upon exiting the orifice throat, the cavities experience a sharp rise in pressure, coupled with an increase in turbulence kinetic energy as the jet enters into the main pipe section and dissipates. The detailed pressure-time history experienced by the cavities is presented in Figure *6*b at pressure ratios of 2.5 & 5.0. The results show that the mean pressure recovery rate is similar for the two pressure ratios, however the amplitude of the pressure fluctuations is indicated to increase significantly as pressure ratio is increased from 2.5 to 5.0. At a pressure ratio of 5, the cavities experience high frequency, high amplitude fluctuations in pressure as they exit the orifice restriction. Influence on l/d ratio on cavity trajectory was also analysed. Lengthening the orifice is shown here to have the effect of controlling and delaying the pressure recovery, subjecting the generated cavities to lower pressures for a longer period. As a sample of results, the detailed pressure time-history is compared for the *l/d* = 5 and *l/d* = 2 cases in Figure *6*c, which highlights the differences in the initial pressure field experienced by the cavity trajectories between the two configurations. For the longer orifice, the low pressure is maintained through the throat which exhibits relative high frequency fluctuations up to the orifice exit plane. Thereafter, the pressure recovery profiles in the main pipe section are broadly similar for the two different configurations, both in terms of the mean and fluctuating components of pressure. Orifice length is therefore a potentially important design parameter in controlling the final cavity collapse conditions, offering a means to control both the pressure recovery rate and oscillation frequency.

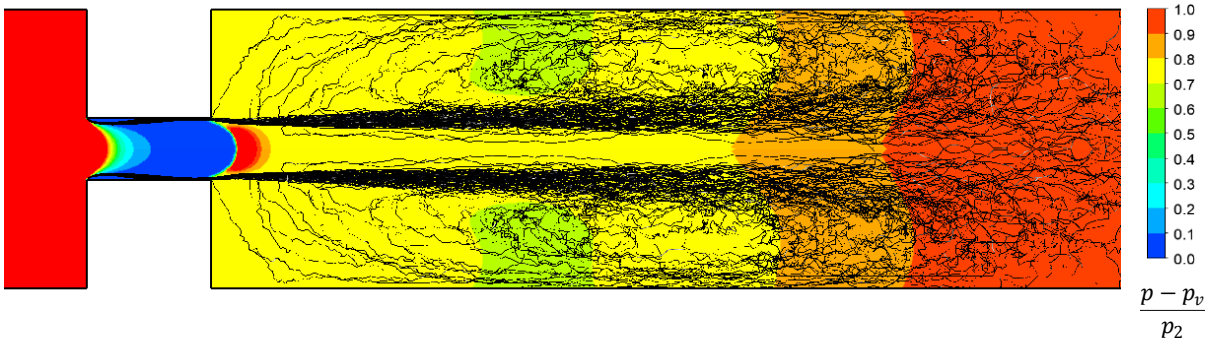

Figure 6a: Discrete cavity trajectories, l/d = 2 (10μm bubble size)

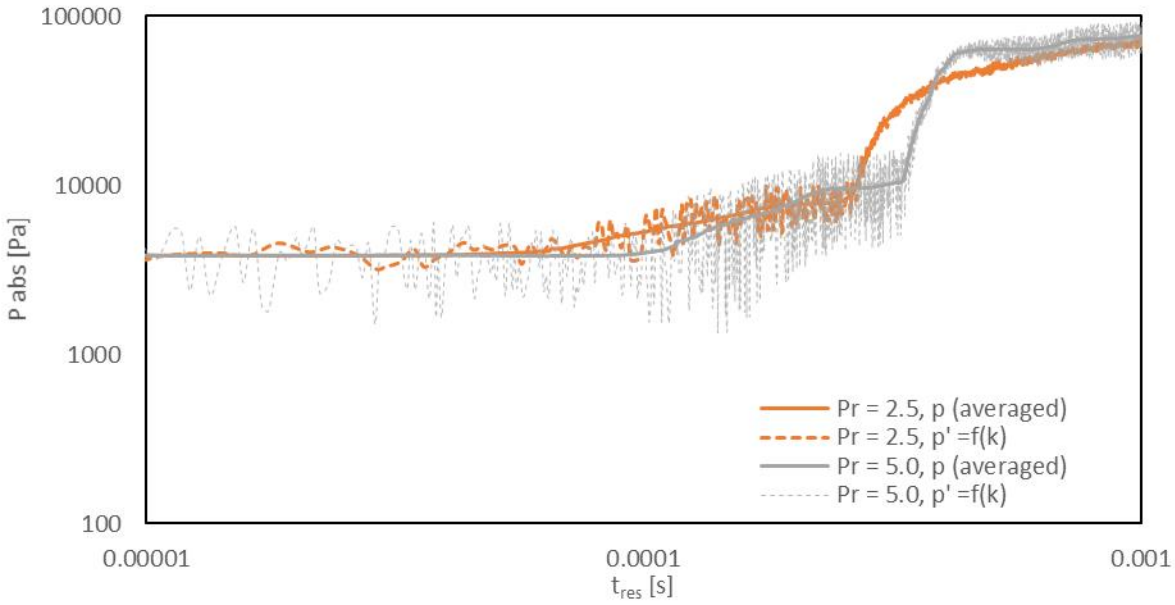

Figure 6b: Influence of pressure ratio on pressure vs time history, l/d = 2.0 (10μm bubble size)

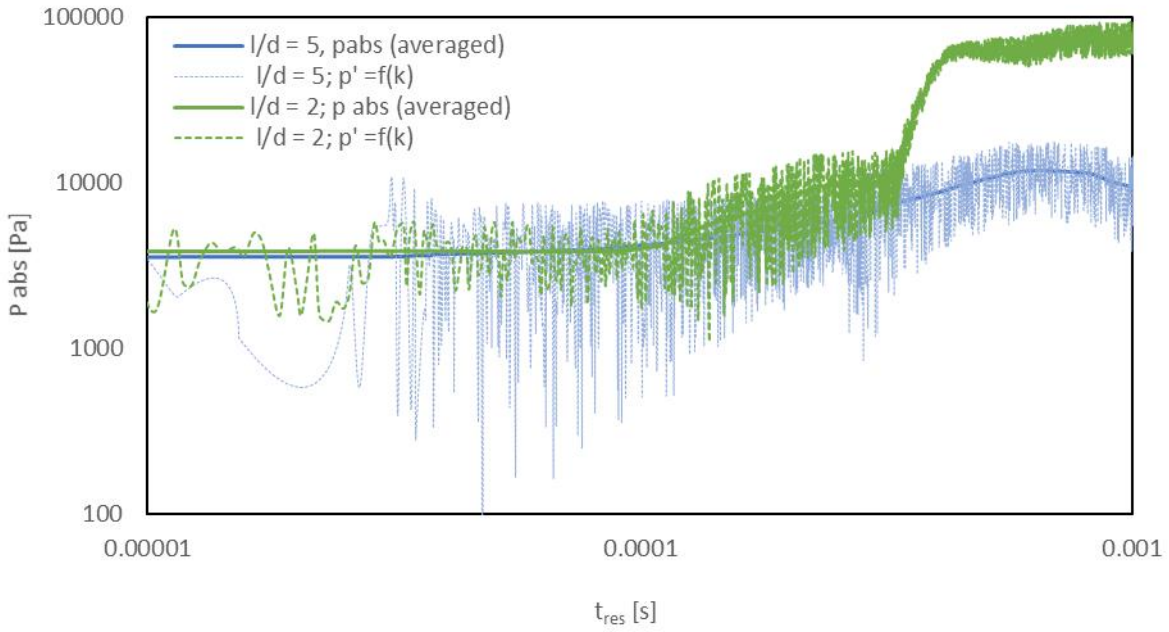

Figure 6c: Influence of l/d ratio on pressure vs time history, pressure ratio = 5 (10μm bubble size)

Figure 6: Influence of l/d ratio on cavity trajectories

3.6 Influence of orifice inlet radius

The sharpness of orifice is also an important parameter influencing characteristic of cavitation. Even a small rounding at the edge can dramatically change the flow field. Simulated flow fields in terms of contours of velocity for the cases with and without an inlet radius are compared in Figure 7a. It can be seen that there are significant differences in the predicted velocity and velocity gradients. At this operating pressure ratio of 1.5 (c_a= 2.2) the inclusion of a small inlet radius of just 0.2mm produces a very local acceleration at the inlet edge, which acts to suppress the separation bubble. Examining the corresponding pressure distribution (Figure 7b), this low acceleration is sufficient to create a local reduction in pressure to the saturated vapour limit. Elsewhere through the throat however, flow acceleration is smoother than that shown for the sharp edged orifice, and pressure losses are lower overall. Similar comparison for turbulence kinetic energy is shown in supplementary information (Figure SI.7). Introduction of a small radius leads to overall reduction in turbulent kinetic energy

values in the shear layer downstream of the orifice exit. The simulated pressure field was examined for different pressure ratios to identify the inception of cavitation. The predicted minimum pressure obtained at various overall pressure ratio for inlet radii of 0.2mm, 1mm and the zero-radius baseline case are shown in Figure SI.8. Using this information, the cavitation inception numbers were calculated for each inlet radius value, and the collated results are presented in Figure 7c. At the larger inlet radii of 1mm, the reduction in velocity gradient is sufficient to delay the predicted onset of cavitation significantly. The subsequent evolution of the vapour cavity at pressure ratios of 2.5 and 5.0 is shown in Figure 7d. Although predicted inception happens at lower pressure ratios for an inlet radius of 0.2mm, the higher separation losses incurred by the sharp edge orifice lead to the development of a larger vapour cavity along the outer wall as pressure ratios are subsequently increased. For the larger inlet radius, the smoothing out of the flow gradients is shown to inhibit the development of cavity formation.

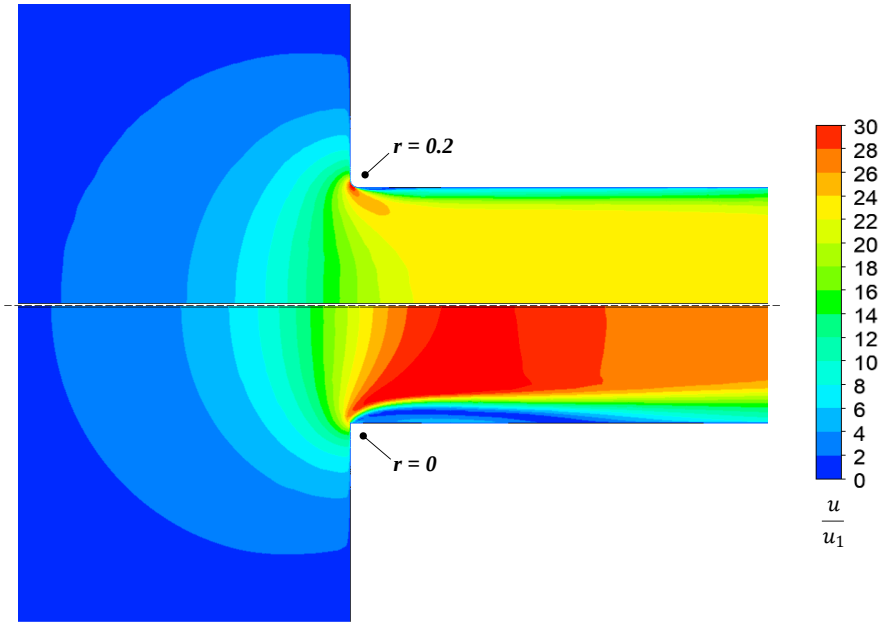

Figure 7a: Velocity contour comparison with different inlet radii

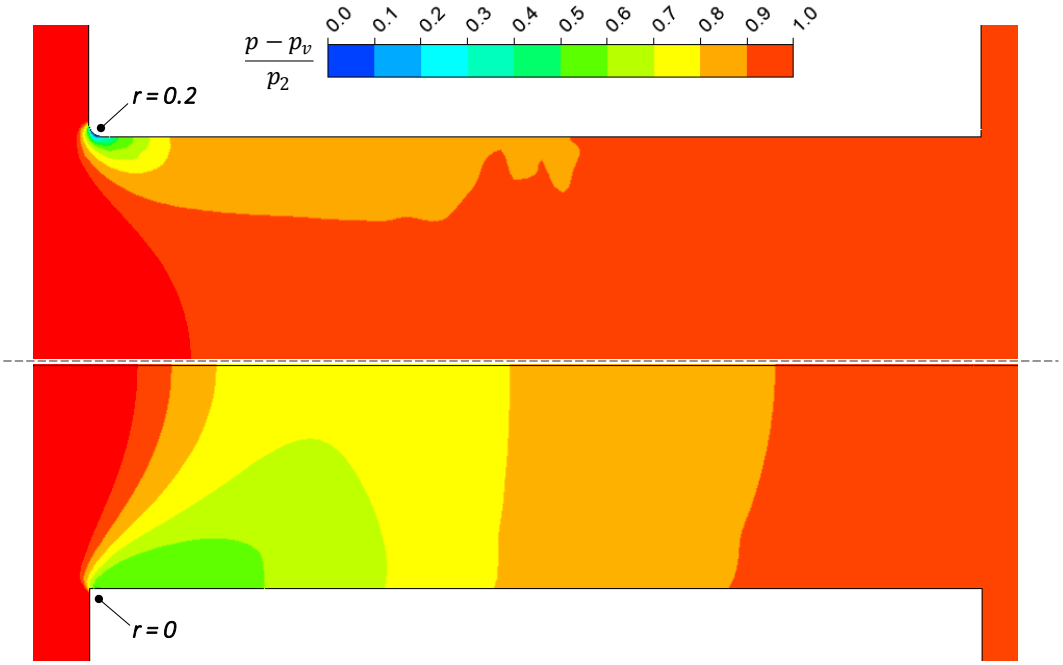

Figure 7b: Comparison of pressure distributions at Pr = 1.5 with different inlet radii

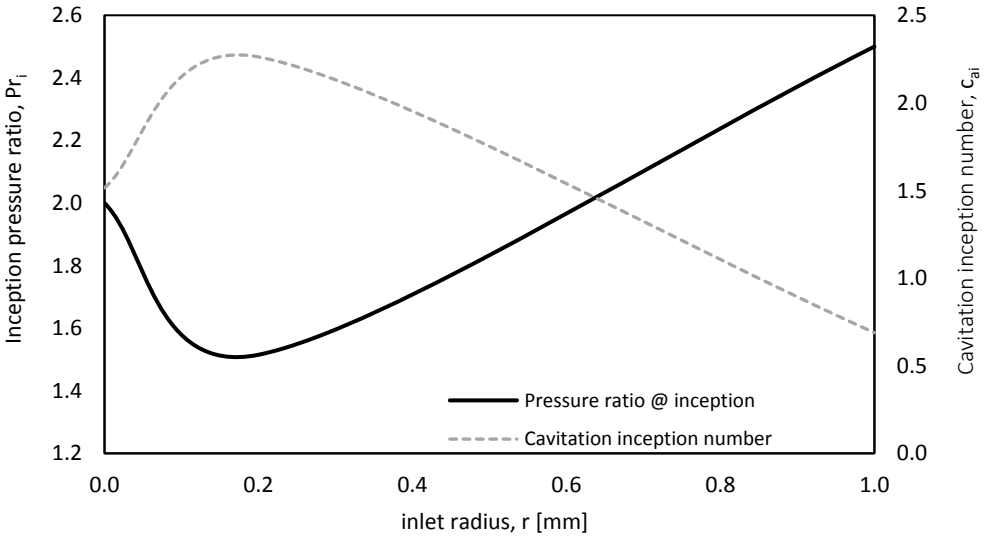

Figure 7c: Cavitation inception number & inception pressure ratio vs inlet radius

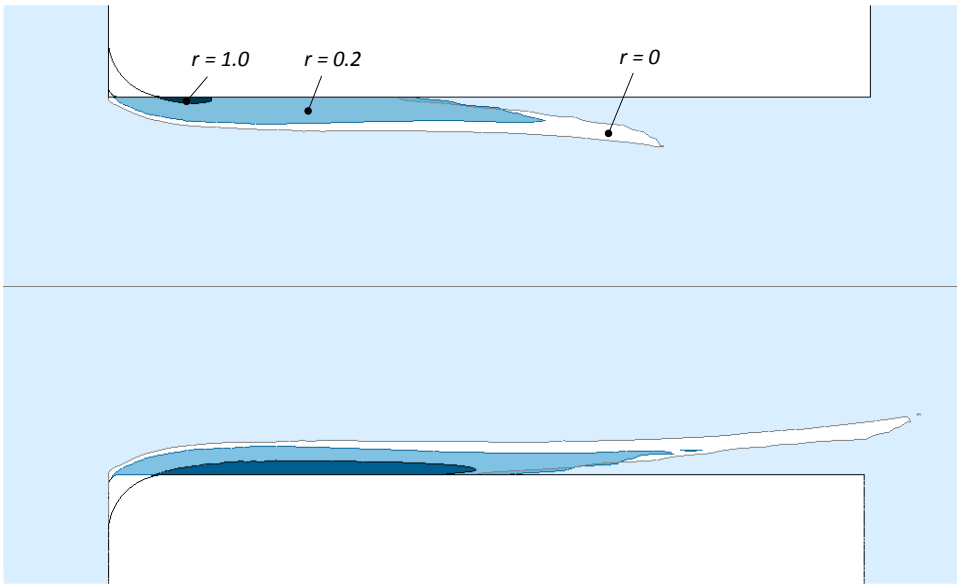

Figure 7d: Iso-surface of vapour volume fraction (= 0.5) for different inlet radii (Pr = 2.5 [top] and Pr = 5.0 [bottom])

Figure 7: Influence of orifice sharpness on cavitating flow

Nurick [18] presented a discussion of the influence of orifice sharpness on cavitation inception. The cavitation inception predicted from the simulated results are compared with the correlation given by Nurick in Figure 8a for the critical cavitation number, $K_{cr,}$ (See Eq.(6), repeated in Figure 8a). The CFD predictions show an initial inflection with the introduction of a very small 0.2mm radius (r/d = 0.03) due to the local acceleration produced unlike the correlation of Nurick. Beyond r/d=0.05, the predictions qualitatively follow the trend indicated by the Nurick correlation. The discharge coefficients of orifices with different sharpness as a function of inlet to outlet pressure ratio are shown in Figure 8b. The results show an inverse relationship between the hydrodynamic efficiency and the extent of vapour mass transfer, which again agrees with previous experimental studies. This highlights the crucial influence of the inlet losses on the generated cavitation activity. The time-pressure histories for an orifice with inlet r/d ratio = 0.2mm are compared with those predicted for the sharp orifice in Figure 8c. Owing to the reduction in turbulent kinetic energy, the addition of a small radius leads to a reduction in the amplitude of the pressure fluctuations at orifice exit.

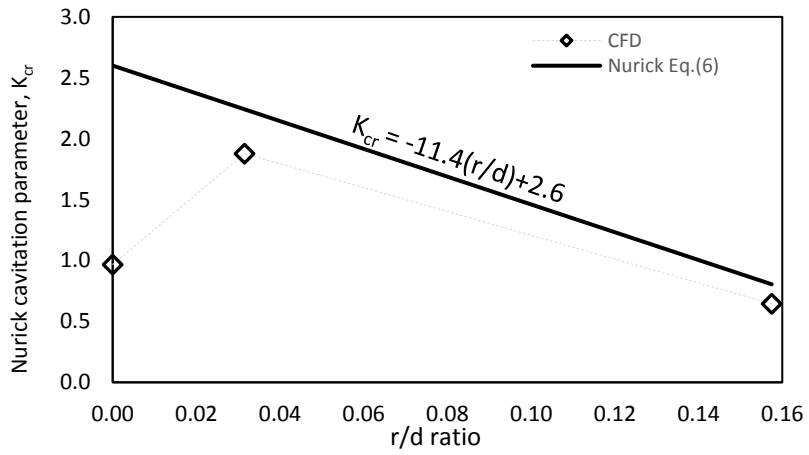

Figure 8a: *Comparison with predicted cavitation inception trend with correlation of Nurick* [18]

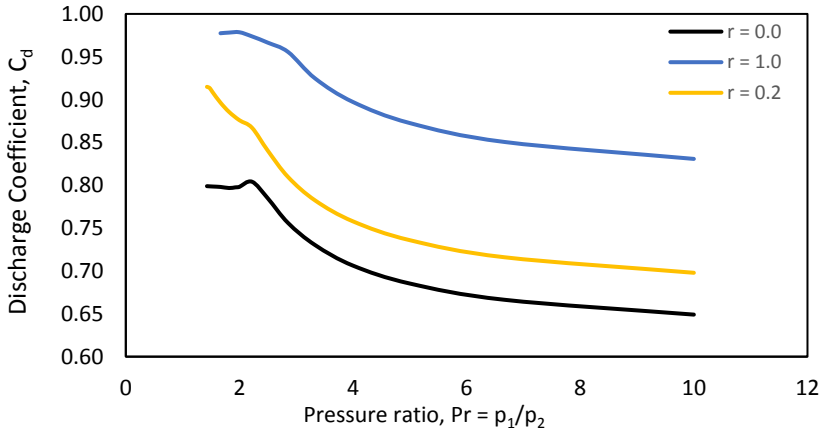

Figure 8b: Discharge coefficient vs pressure ratio for varying inlet radii

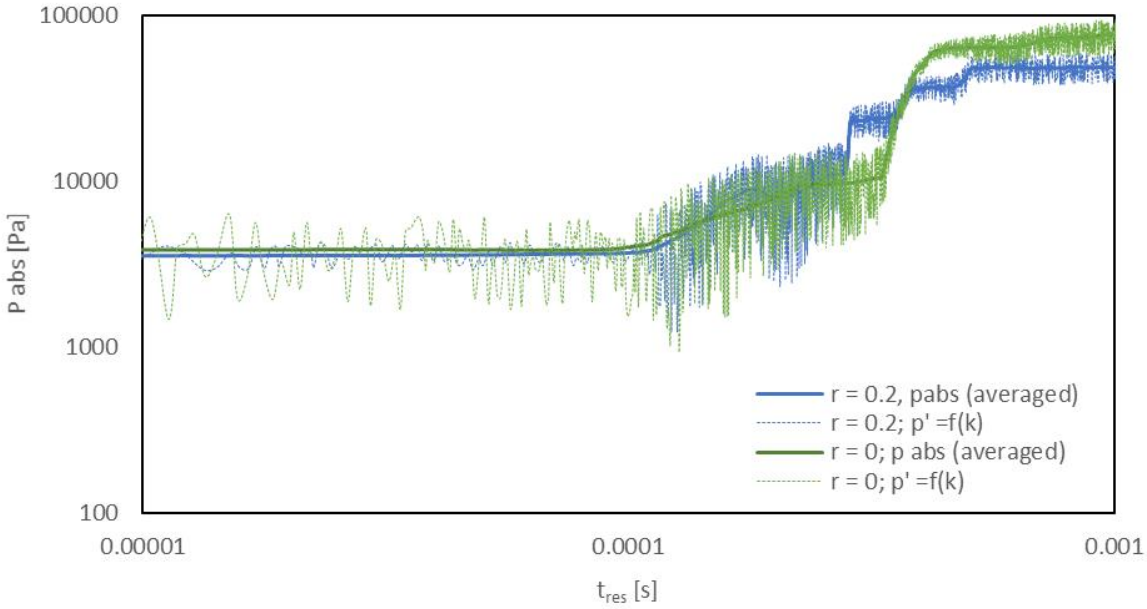

Figure 8c: Influence of l/d ratio on pressure vs time history, pressure ratio = 5.0

Figure 8: Influence of orifice sharpness on cavitation inception, discharge coefficients and cavity trajectories

3.7 Influence of orifice hole angle

For a given thickness of orifice, whether the orifice hole is flat or converging or diverging may also influence the resulting flow field and cavitation. For an orifice with *l/d*=0.5, the predicted velocity distributions for three different orifice outer wall profiles; one with a low entry loss converging 45° conical section, a straight section, and a 45° diverging section are shown in Figure 9a. The sign convention adopted denotes a converging, or decreasing area formed by the wall as a positive (+) hole angle, and a diverging section denoted as negative (-). The corresponding pressure fields are presented in Figure 9b. As would be expected the converging section has the effect of minimising the separation bubble in comparison to both the straight and diverging section geometries. However the pressure ratios required for cavitation inception are higher than that required for the straight section. Figure 9c shows the minimum predicted pressure in the device versus operating pressure ratio. The corresponding cavitation inception numbers, determined from the conditions at which the minimum predicted pressure reaches the saturated vapour pressure, were found to be 0.66, 0.91 & 1.16 for the +45°, -45° and 0° straight section respectively. Both angle profile sections require much higher pressure ratios (30 – 40%) to drive the minimum pressure towards the saturated vapour pressure; this would suggest a significant impact on overall energy efficiency and consumption.

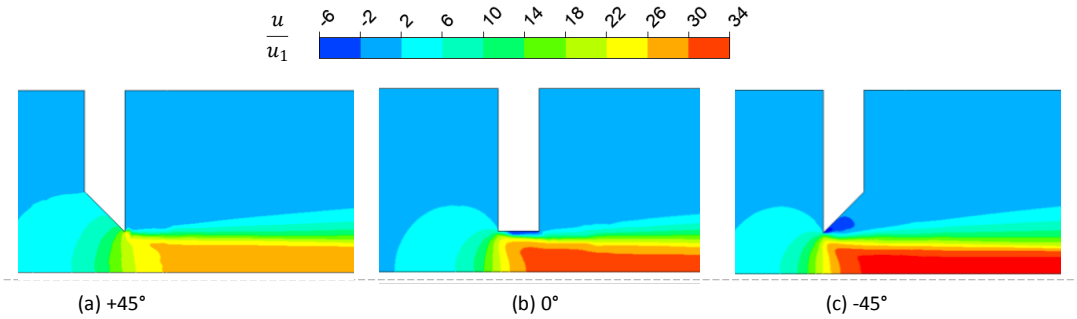

Figure 9a: Velocity contours with varying orifice angle (pressure ratio =5.0)

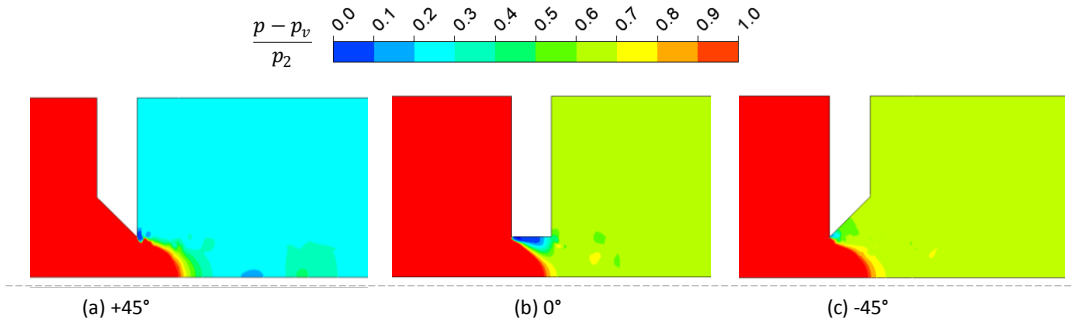

Figure 9b: Pressure contours with varying orifice angle (pressure ratio = 5.0)

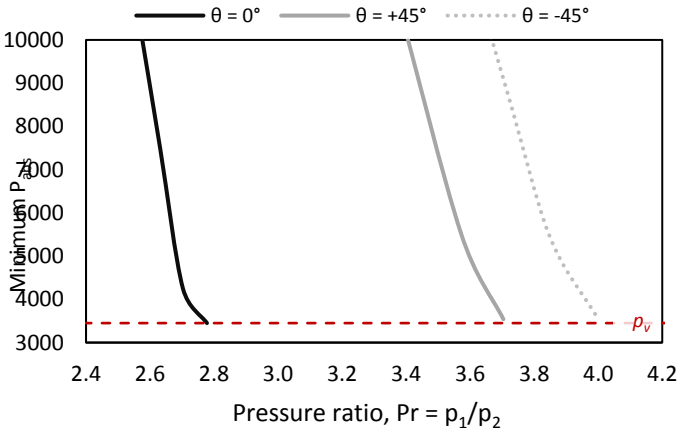

Figure 9c: Minimum pressure vs pressure ratio with varying orifice angles

Figure 9: Influence of orifice hole angle on cavitating flow

4 Conclusions

Computational fluid dynamics models were developed to simulate cavitating flow through orifice. Influence of key design and operating parameters were investigated. The simulated results on discharge coefficient and cavitation inception were compared with the published experimental data wherever possible. The validated model was used to decipher trends in the variation of cavitation onset and extent with varying design inputs. The presented model and results will be useful to evolve optimum design parameters to achieve maximum levels of cavitational activity for given flow rate / pressure ratio requirements. The hydrodynamic conditions experienced by individual vapour cavities was also quantified and compared across different designs, and at different operating conditions. The key findings of this investigation are as follows:

- The cavitation model of Singhal [30] is able to describe two phase flow in a range of orifice designs. Comparison with experimental data available in open literature shows good levels of agreement in predicted pressure ratio versus flow rate behaviour in the cavitating regime, including the transition to choked flow at high flow rates.
- Of the design parameters investigated in this work, the orifice thickness has the most pronounced influence on cavitation inception and extent. Minimum l/d values of 2.0 are suggested, below which cavitation inception requires higher pressure ratios and flow rates. A factor of 10 difference in pressure ratio required to initiate cavitation was found over the l/d range 0-5.
- Above l/d ratios of 2, increasing orifice thickness controls the pressure recovery rate experienced by the generated cavities, suggesting that this is parameter may play an important role in controlling the final collapse conditions.
- Comparing cavitation inception numbers across different designs shows a wide variation; with increasing orifice thickness the cavitation inception number was found to vary from 0.2 up to 1.5.
- Inlet rounding also has a considerable influence on cavitation behaviour; sharp edged orifice designs are more effective in initiating cavitation, with larger values of the order of 1mm showing delayed inception and thereafter attenuated growth. This has consequences when considering erosion at the orifice inlet, as this may lead to rounding and thus a potentially significant change in cavitation behaviour.
- Orifice designs featuring angled walls are similarly predicted to require higher pressure ratios and flow rates to generate cavitation in comparison to a constant area (straight) throat section.
- Trajectory simulations indicate that mean pressure recovery rates appear to be relatively insensitive to overall pressure ratio. Increasing the pressure ratio however significantly increases the amplitude of the turbulent fluctuations experienced by discrete cavities as they exit the orifice.

The models and results presented in this work offer a means to link single cavity simulations to the output from CFD models, and thus compare the collapse pressures and temperatures obtained with different geometries and process inputs. These results will be discussed separately. The presented approach and results provide useful insights for designing and optimising appropriate hydrodynamic cavitation devices based on orifices.

Nomenclature

d	Orifice hole diameter	[mm]
k	Turbulent kinetic energy	[m^2/s^2]
l	Orifice hole length	[mm]
n	Bubble number density	
r	Orifice hole inlet radius	[mm]
$u,$	Velocity [m/s]	
x	Distance	[mm]
c_a	Cavitation number	
c_{ai}	Cavitation inception number	
C_c	Contraction coefficient	
C_d	Discharge coefficient	
D	Orifice pipe internal diameter	[mm]
K	Cavitation parameter (From Pierce et al. [17])	
Kcr	Critical cavitation parameter	
p	Pressure	[Pa]
Pr	Pressure ratio (inlet / outlet)	
Pr_i	Inception pressure ratio (inlet / outlet)	
R		
T_L	Particle eddy lifetime	[s]
We	Webber number	

Greek symbols:

α	Volume fraction	
ε	Turbulence dissipation rate	[m^2/s^3]
θ	Orifice wall angle	[°]
$\sigma,$	Surface tension	
ρ	Density	[kg/m^3]
μ	*Dynamic viscosity*	[Pa.s]
ω	Turbulence dissipation rate	[s^{-1}]
ζ	Normally distributed random number	
Γ	Diffusivity	[m^2/s]

Subscripts:

1	Inlet / upstream location
2	Outlet / downstream recovered pressure location
a	Absolute
B	Bubble
ch	Characteristic
t	Orifice throat
l	Liquid
v	Vapor
g	Non condensable gas (NCG)
m	Mixture
p	Particle
rel	Relative

References:

[1] Ranade V V and Bhandari V M 2014 *Industrial Wastewater Treatment, Recycling and Reuse* (Elsevier)

[2] Braeutigam P, Wu Z L, Stark A and Ondruschka B 2009 Degradation of BTEX in aqueous solution by hydrodynamic cavitation *Chem. Eng. Technol.* **32** 745–53

[3] Kalumuck K M and Chahine G L 1998 the Use of Cavitating Jets To Oxidize Organic Compounds in Water *Proc. FJIDSM ASME Fluids Eng. Div. Summer Meet. June -,, Washington, DC* **122** 1–10

[4] Musmarra D, Prisciandaro M, Capocelli M, Karatza D, Iovino P, Canzano S and Lancia A 2016 Degradation of ibuprofen by hydrodynamic cavitation: Reaction pathways and effect of operational parameters *Ultrason. Sonochem.* **29** 76–83

[5] Zupanc M, Kosjek T, Petkovšek M, Dular M, Kompare B, Širok B, Blažeka Ž and Heath E 2013 Removal of pharmaceuticals from wastewater by biological processes, hydrodynamic cavitation and UV treatment *Ultrason. Sonochem.* **20** 1104–12

[6] Bhandari V M, Sorokhaibam L G and Ranade V V. 2016 Industrial wastewater treatment for fertilizer industry—A case study *Desalin. Water Treat.* **57** 27934–44

[7] Patil P N, Bote S D and Gogate P R 2014 Degradation of imidacloprid using combined advanced oxidation processes based on hydrodynamic cavitation *Ultrason. Sonochem.* **21** 1770–7

[8] Joshi R K and Gogate P R 2012 Degradation of dichlorvos using hydrodynamic cavitation based treatment strategies *Ultrason. Sonochem.* **19** 532–9

[9] Arrojo S, Benito Y and Martínez Tarifa A 2008 A parametrical study of disinfection with hydrodynamic cavitation *Ultrason. Sonochem.* **15** 903–8

[10] Maddikeri G L, Gogate P R and Pandit A B 2014 Intensified synthesis of biodiesel using hydrodynamic cavitation reactors based on the interesterification of waste cooking oil *Fuel* **137** 285–92

[11] Kelkar M A, Gogate P R and Pandit A B 2008 Intensification of esterification of acids for synthesis of biodiesel using acoustic and hydrodynamic cavitation *Ultrason. Sonochem.* **15** 188–94

[12] Terán Hilares R, de Almeida G F, Ahmed M A, Antunes F A F, da Silva S S, Han J I and Santos J C dos 2017 Hydrodynamic cavitation as an efficient pretreatment method for lignocellulosic biomassA parametric study *Bioresour. Technol.* **235** 301–8

[13] Nakashima K, Ebi Y, Shibasaki-Kitakawa N, Soyama H and Yonemoto T 2016 Hydrodynamic Cavitation Reactor for Efficient Pretreatment of Lignocellulosic Biomass *Ind. Eng. Chem. Res.* **55** 1866–71

[14] Carpenter J, George S and Saharan V K 2017 Low pressure hydrodynamic cavitating device for producing highly stable oil in water emulsion: Effect of geometry and cavitation number *Chem. Eng. Process. Process Intensif.* **116** 97–104

[15] Zhou Z a., Xu Z, Finch J a., Hu H and Rao S R 1997 Role of hydrodynamic cavitation in fine particle flotation *Int. J. Miner. Process.* **51** 139–49

[16] Vichare B N P, Gogate P R and Pandit A B 2000 Full Papers Optimization of Hydrodynamic Cavitation Using a Model *Chem. Eng. Technol.* **23** 683–90

[17] Pearce I D and Lichtarowicz A 1971 Discharge Performance of Long Orifices with Cavitating Flow *Second Fluid Power Symposium, Paper D2, British Hydromechanics Research Association, Fluid Engineering, Guildfod, U.k.*

[18] Nurick W H 1976 Orifice Cavitation and Its Effect on Spray Mixing *J. Fluids Eng.* **98** 681

[19] Ohrn, T.R., Senser, D.W., Lefebvre A H 1991 Geometrical effects on discharge coefficients for pain-orifice atomizers *At. Sprays* **1** 137–53

[20] Ramamurthi K and Nandakumar K 1999 Characteristics of flow through small sharp-edged cylindrical orifices *Flow Meas. Instrum.* **10** 133–43

[21] Carpenter J, Badve M, Rajoriya S, George S, Saharan V K and Pandit A B 2017 Hydrodynamic cavitation: An emerging technology for the intensification of various chemical and physical processes in a chemical process industry *Rev. Chem. Eng.* **33** 433–68

[22] Braeutigam P, Franke M, Wu Z-L and Ondruschka B 2010 Role of Different Parameters in the Optimization of Hydrodynamic Cavitation *Chem. Eng. Technol.* n/a-n/a

[23] Šarc A, Stepišnik-Perdih T, Petkovšek M and Dular M 2017 The issue of cavitation number value in studies of water treatment by hydrodynamic cavitation *Ultrason. Sonochem.* **34** 51–9

[24] Hickel S 2015 DNS and LES of two-phase flows with cavitation *ERCOFTAC Ser.* **20** 595–604

[25] Menter F R 1994 Two-equation eddy-viscosity turbulence models for engineering applications *AIAA J.* **32**

[26] Bardina, J.E., Huang, P.G., Coakley T J 1997 Turbulence modelling validation *AIAA-1997-2121*

[27] Ansys 2016 Ansys Inc, FLUENT 17.0 Theory Guide

[28] Schnerr G H and Sauer J 2001 Physical and Numerical Modeling of Unsteady Cavitation Dynamics *Fourth Int. Conf. Multiph. Flow* 1–12

[29] Zwart P J, Gerber A G and Belamri T 2004 A Two-Phase Flow Model for Predicting Cavitation Dynamics

Fiifth International Conference on Multiphase Flow, Yokohama, Japan
[30] Singhal A K, Athavale M M, Li H and Jiang Y 2002 Mathematical Basis and Validation of the Full Cavitation Model *J. Fluids Eng.* **124** 617
[31] Ebrahimi B, He G, Tang Y, Franchek M, Liu D, Pickett J, Springett F and Franklin D 2017 Characterization of high-pressure cavitating flow through a thick orifice plate in a pipe of constant cross section *Int. J. Therm. Sci.* **114** 229–40
[32] Brennan C E 1995 *Cavitation and Bubble Dynamics* (Oxford University Press: New York)
[33] Alehossein H and Qin Z 2007 Numerical analysis of Rayleigh-Plesset equation for cavitating water jets *Int. J. Numer. Meth. Engng.* **72** 780–807